Supporting Information for

Vapor-deposited Nanotwinned Copper Thin Film Enhances C_2 Production in CO_2 Electroreduction

Juntai Shen[1#], Xiang Yao[2#], Qingye Ren[1], Tianxiang Jiang[3] Langli Luo[1*], Lifeng Zhang[1*]

[1] *Institute of Molecular Plus, Department of Chemistry, Tianjin University, Tianjin 300072, China.*

[2] *Institute of Biomedical Engineering, Chinese Academy of Medical Science & Peking Union Medical College Tianjin 300192, China.*

[3] *The Institute of Seawater Desalination and Multipurpose Utilization, Ministry of Natural Resources, Tianjin 300192, China.*

†Equally contributed first author

*Corresponding author: Lifeng Zhang (lfzhang007@tju.edu.cn), Langli Luo (luolangli@tju.edu.cn).

Experimental

Reagents and materials: The Cu target (99.999%) was purchased from Fuzhou Yingfeixun Optoelectronics Technology®. Potassium bicarbonate ($KHCO_3$) was purchased from Aladdin®. All chemical reagents were used as received without further purification. Fabrication of Cu film: The copper films were prepared using a vacuum thermal evaporation system FS380 from Suzhou Fangsheng Optoelectronics Co., Ltd. under vacuum conditions using quartz with high roughness as the substrate. The power was increased by 36 % at a rate of 1.5 % per minute and followed by a subsequent increase of 1 % per minute to 40 %. The deposition process was then kept at a rate of 0.1 $Å \cdot s^{-1}$ and continued until the desired film thickness was achieved. The deposition rate and film thickness were monitored using quartz monitor crystals. Annealing of Cu films: The annealing of the Cu films was carried out using a tube furnace with hydrogen and argon protection at 250 ℃ for 60 minutes, 90 minutes and 120 minutes.

Characterization of materials: X-ray diffraction using Cu Kα radiation as the radiation source through the Rigaku Smartlab® 9 kW. Scanning electron microscopy images were obtained using a Thermo Scientific® Apreo scanning electron microscope. The surface composition of the Cu film was investigated by X-ray photoelectron spectroscopy (XPS, ThermoScientific® K-Alpha instrument) and Auger electron spectroscopy (AES). AES depth profiles were obtained by etching the surface of the catalysts using an argon ion beam, resulting in a depth of 4 nm. The TEM and high-angle annular dark-field (HAADF)- and low angle annular dark-field (DF2)-STEM images were obtained using a Thermo Scientific® Talos F200X transmission electron microscope with an acceleration voltage of 200 kV.

Electrochemical measurements: The CO_2RR electrochemical measurements were performed in the carbon dioxide saturated 0.1 M $KHCO_3$ aqueous solution using a customized gastight H-type glass cell separated by a Nafion 117 membrane. Each chamber was filled with 30 mL of a 0.1 M $KHCO_3$ solution. A piece of Pt foil (2cm×2cm×0.2cm) electrode as the counter electrode and a KCl-saturated Ag/AgCl electrode as the reference electrode, and the Cu films (≈1cm×1cm) served as the working electrode. Before the reaction, the 0.1 M $KHCO_3$ aqueous solution was purged

with carbon dioxide for 30 minutes to saturate the solution (pH=6.8). All electrochemical data including cyclic voltammetry, linear sweep voltammetry and current-time (i-t) measurements, were recorded using CHI®660E electrochemical workstation. During the electrochemical reaction, CO_2 was continuously purged at 30 sccm, regulated by a mass flow controller, and controlled potential electrolysis was conducted to perform the electrochemical reduction of CO_2. All potentials were calibrated to the RHE scale as follows: $V_{RHE} = V_{Ag/AgCl} + 0.197\ V + 0.0059 \times pH - i \times R_{\Omega}$. The Ohmic drop ($R_{\Omega}$), determined by electrochemical impedance spectroscopy, was corrected automatically 50% by electrochemical workstation, and the remainder was corrected manually.

After the gas steam passed through the cell, it was directly introduced into a gas chromatograph (GC, Shimadzu® GC 2030) equipped with a BID detector for product separation and analysis. High purity He gas was used as the carrier gas for the GC. The concentration of product gases was determined using calibration curves from standard gases. Faradaic efficiency can be calculated as follows:

$$FE = \frac{z_i \times V_i \times V \times p \times F}{R \times T \times I}$$

Where z_i is the number of electrons transferred to produce a molecule; V_i is the measured volume concentration of product i; V is the CO_2 flow rate (30 mL·min^{-1}); p is the atmospheric pressure (1.013×105 Pa); F is the Faradaic constant (96485 C·mol^{-1}); R is the ideal gas constant (8.314 J·mol^{-1}·K^{-1}); T is the reaction temperature (298 K); I is the current measured by the electrochemical workstation.

Figures and Tables

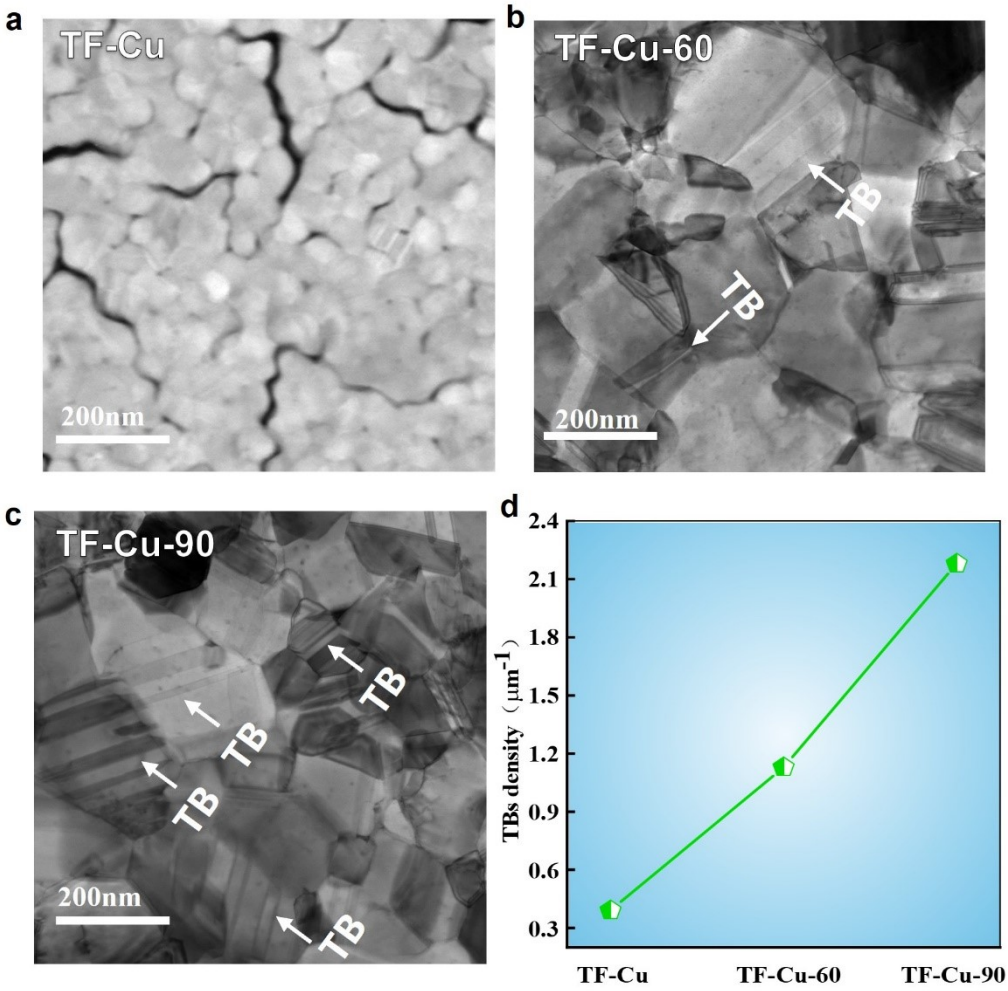

Fig. S1 (a-c) HAADF-STEM images of TF-Cu catalysts with different annealing conditions. The regions indicated by white arrows are twin structures. (d) Statistical result of the twin boundary density for TF-Cu, TF-Cu-60 and TF-Cu-90 catalysts, which was measured by twin boundary length per square nanometer.

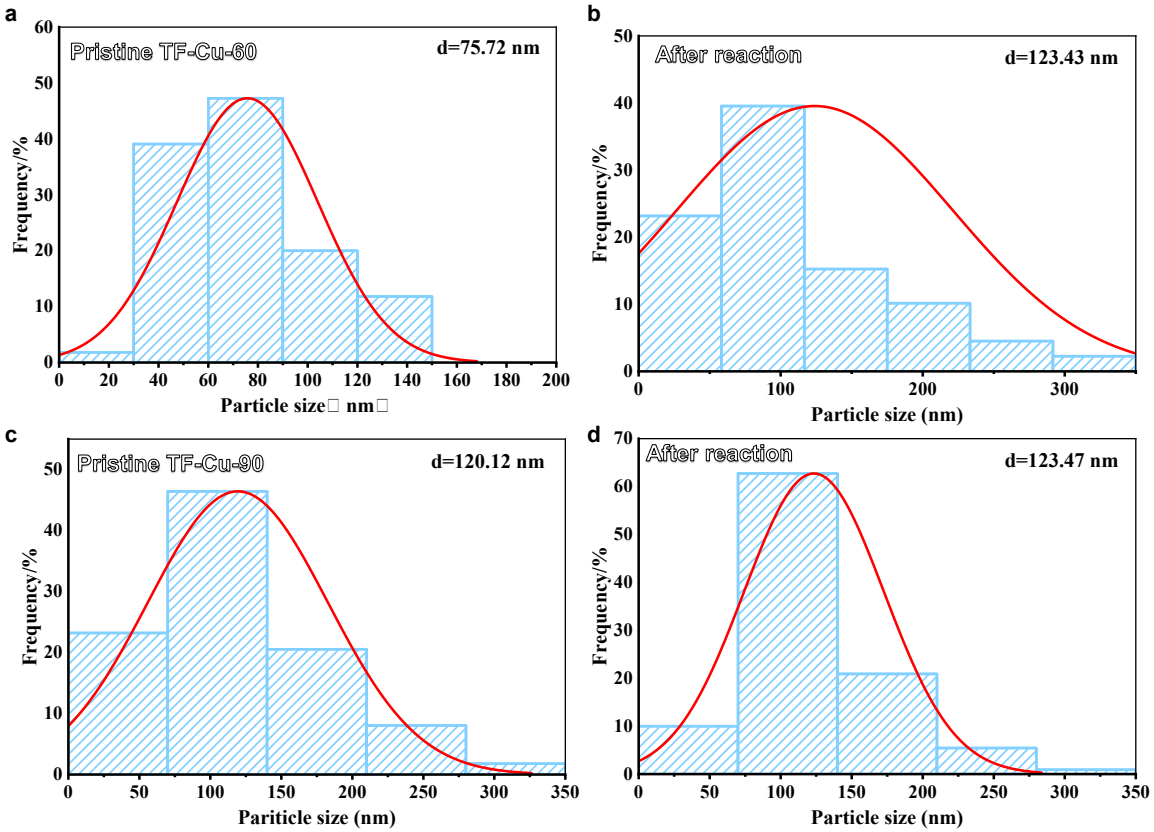

Fig. S2 Grain size distribution of TF-Cu-60 (a,b) and TF-Cu-90 (c,d) catalysts before (a,c) and after (b,d) reaction.

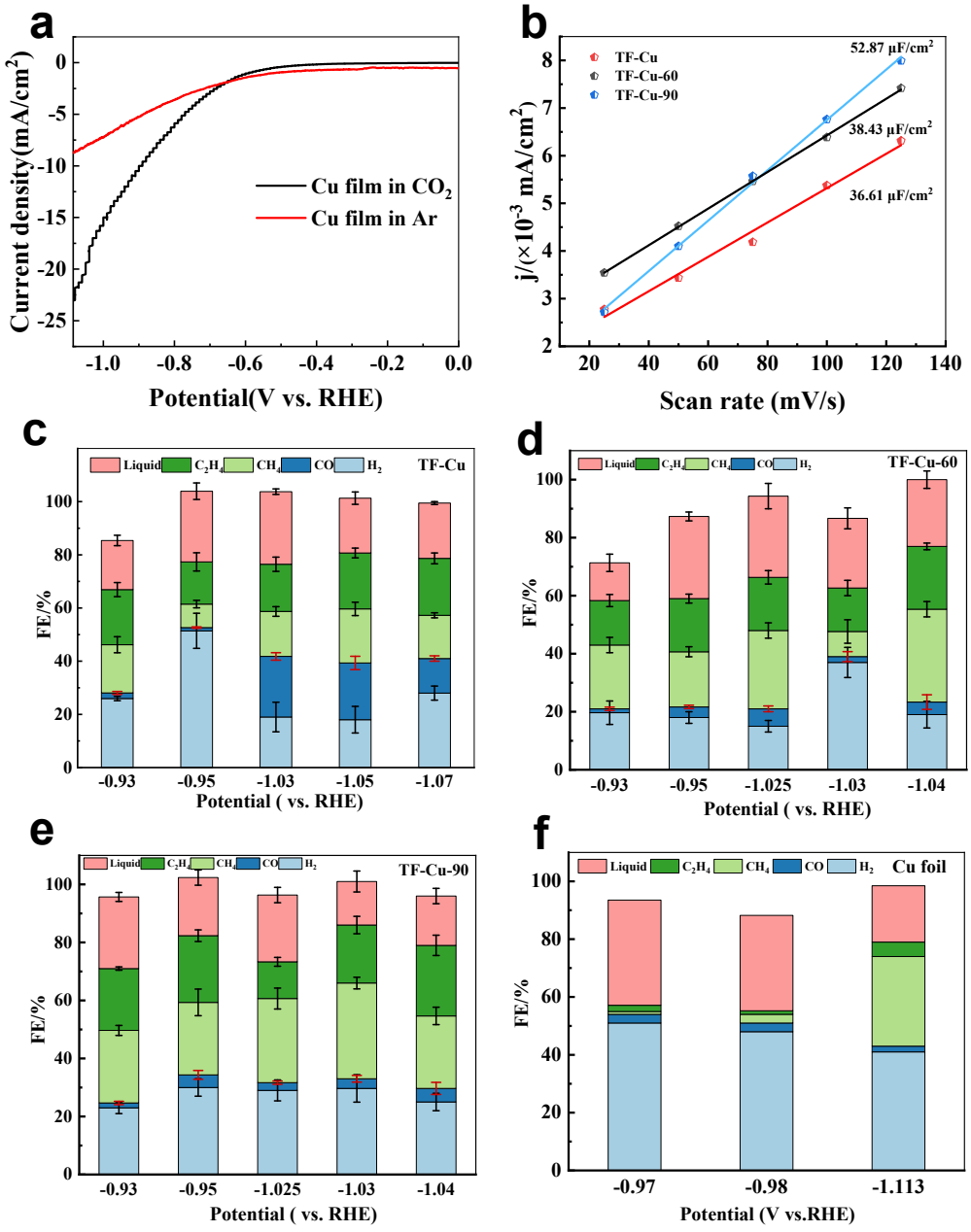

Fig. S3 Electrochemical performance of TF-Cu and Cu foil. (a) Linear sweep voltammetry (LSV) curves of TF-Cu in CO_2-saturated and Ar-saturated 0.1 M $KHCO_3$ aqueous electrolyte. (b) Double-layer capacitance plots of TF-Cu-0, TF-Cu-60, and TF-Cu-90. Electrocatalytic CO_2 reduction performance of (c) TF-Cu, (d) TF-Cu-60, (e) TF-Cu-90 and (f) Cu foil in CO_2-saturated 0.1 M $KHCO_3$. All electrochemical measurements were carried out in 0.1 M $KHCO_3$ at 298 K.

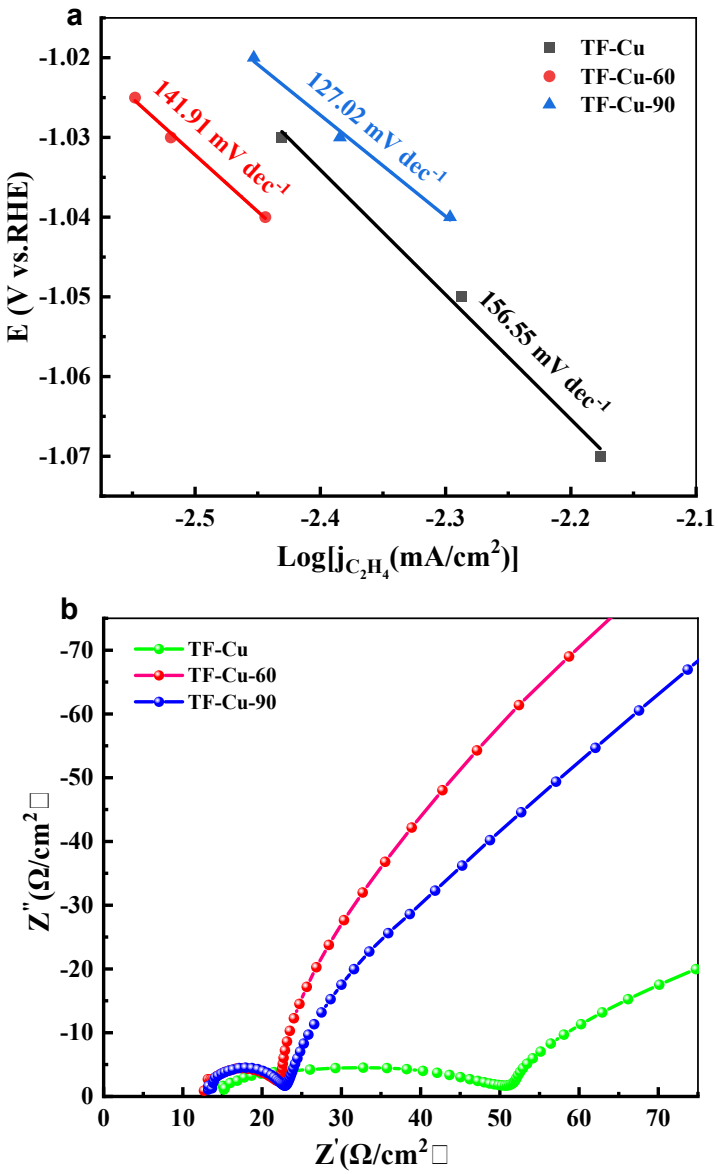

Fig. S4 (a). Tafel plots of TF-Cu, TF-Cu-60, and TF-Cu-90 for the CO_2 reduction reaction. (b). Nyquist plots obtained from electrochemical impedance spectroscopy (EIS) measurements of TF-Cu, TF-Cu-60, and TF-Cu-90. The Tafel slopes were obtained by linear fitting of the linear regions in the plots of E versus $\log_{10}(|j|)$. The Tafel slopes were determined from the selected potential window and were found to decrease from 156.55 mV dec^{-1} for TF-Cu, to 141.91 mV dec^{-1} for TF-Cu-60, and further to 127.02 mV dec^{-1} for TF-Cu-90. The charge-transfer resistance values of TF-Cu-60 and TF-Cu-90 are comparable, suggesting that the superior catalytic performance of TF-Cu-90 cannot be explained solely by a further decrease in charge-transfer resistance.

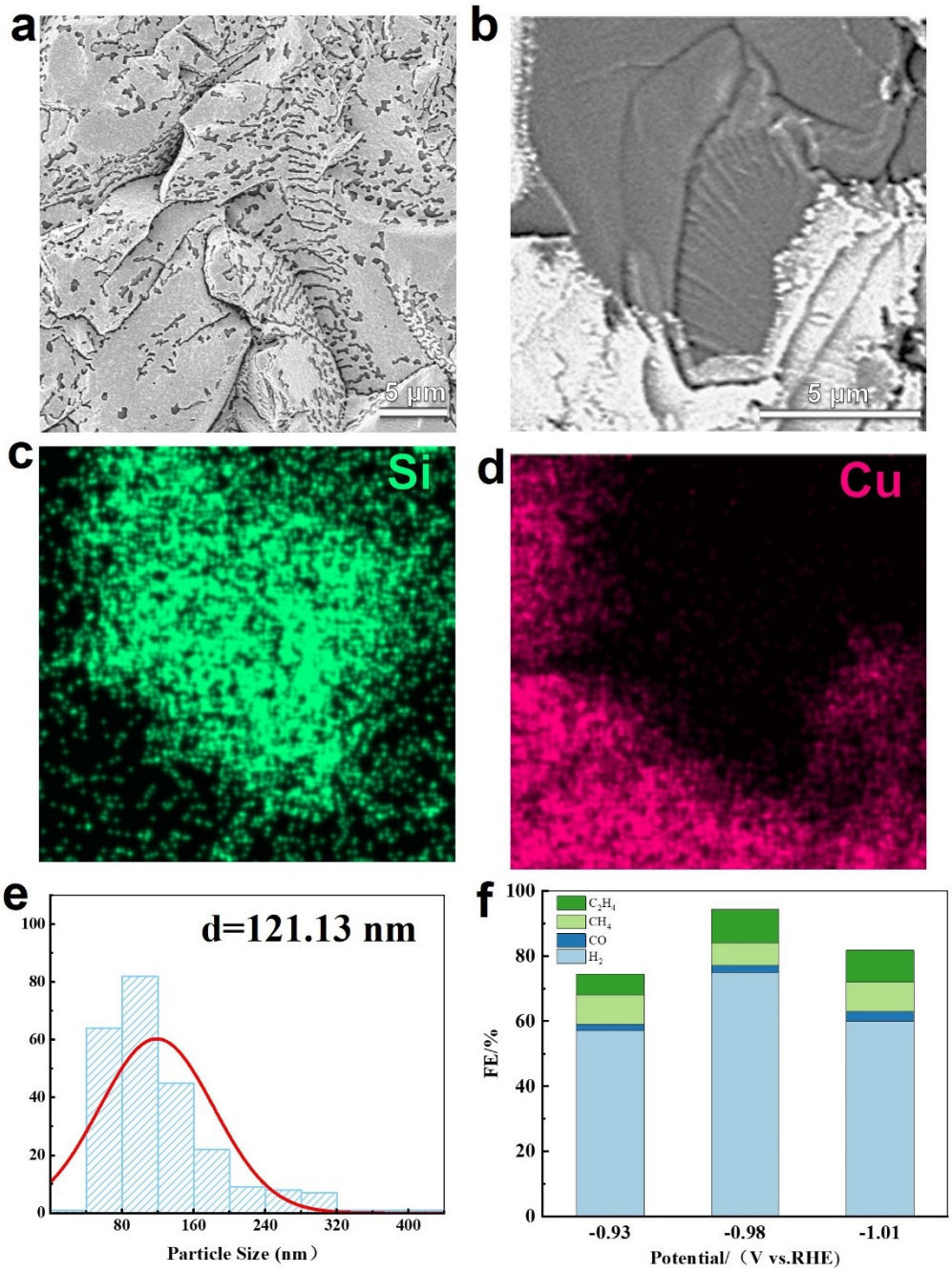

Fig. S5 (a,b) SEM images of the TF-Cu-120 sample at different magnifications. (c,d) Corresponding EDS elemental maps of the region marked in panel b. (e) Grain size distribution histogram of TF-Cu-120. (f) Faradaic efficiencies of TF-Cu-120 for CO_2 reduction products at different applied potentials.

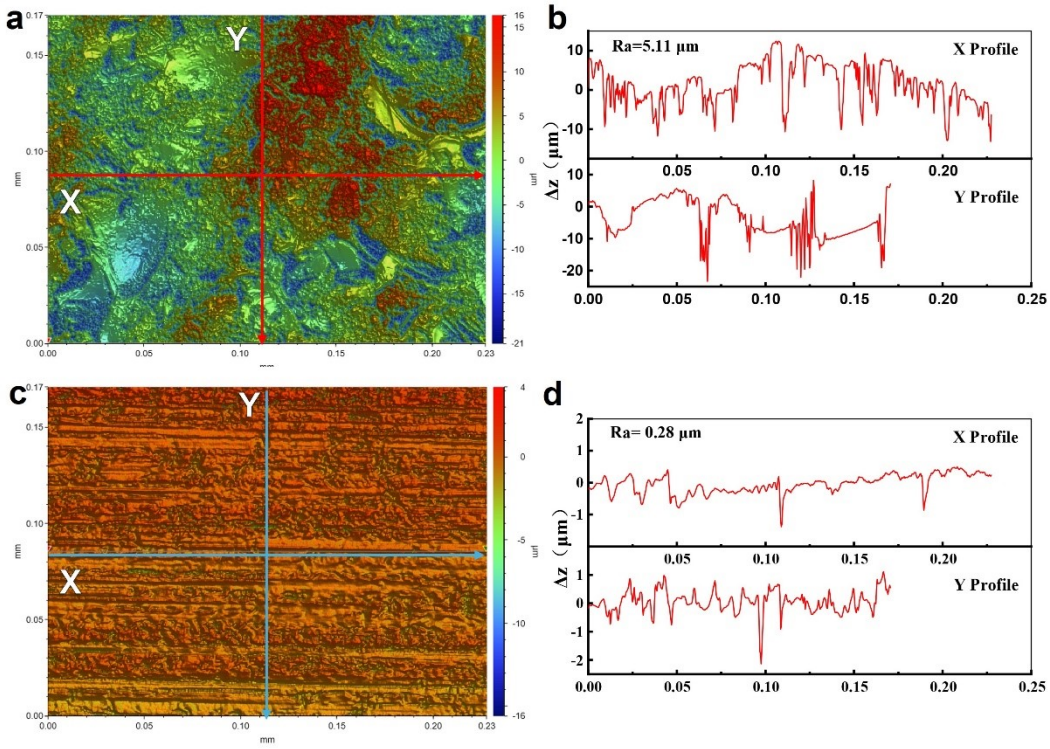

Fig. S6 Surface roughness measurement of the TF-Cu and the Cu foil. (a, c) Optical profilometry topography map of the vapor-deposited thin film Cu (TF-Cu) and commercial Cu foil. (b, d) Corresponding X and Y line profiles along the regions along "X" and "Y" arrows in Fig. S1(a,c).

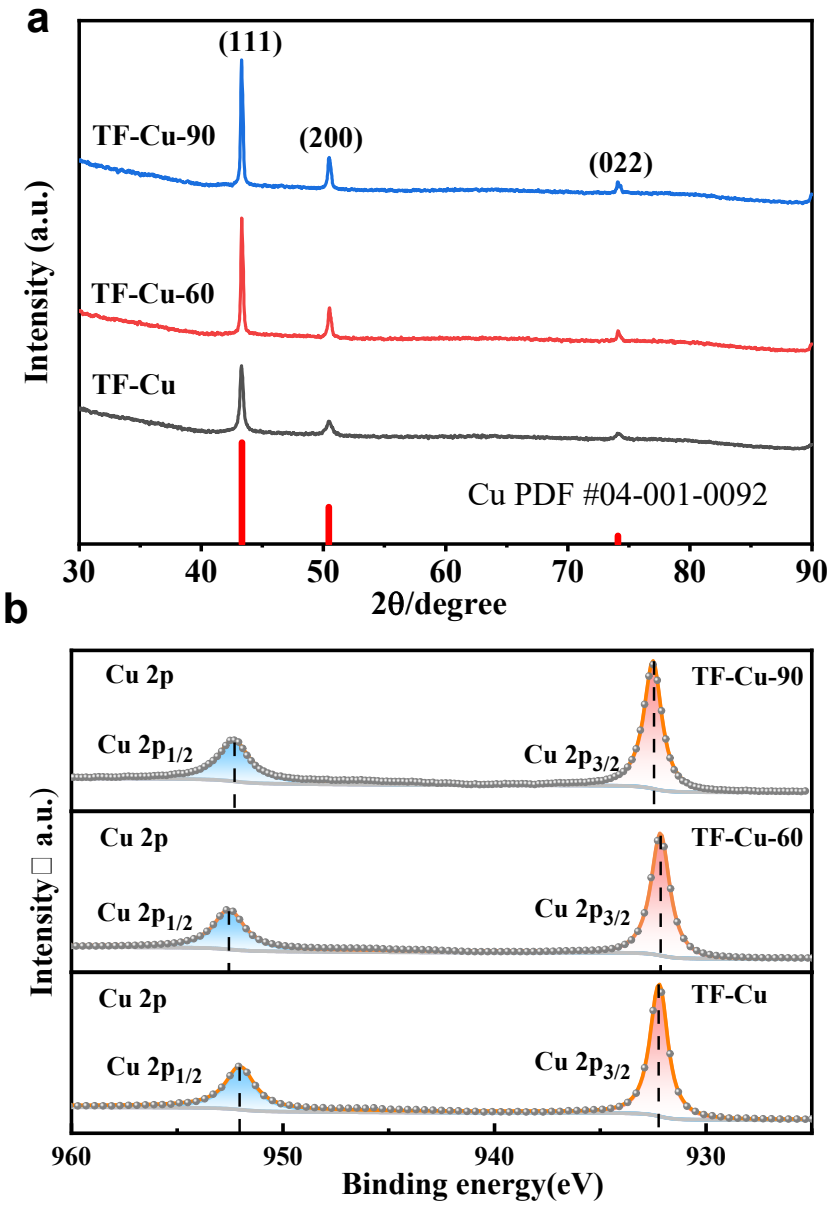

Fig. S7 XRD and XPS of TF-Cu under different annealing times. (a) XRD of TF-Cu, TF-Cu-60 and TF-Cu-90 before reaction. (b). Cu 2p XPS of TF-Cu, TF-Cu-60 and TF-Cu-90 after etching.

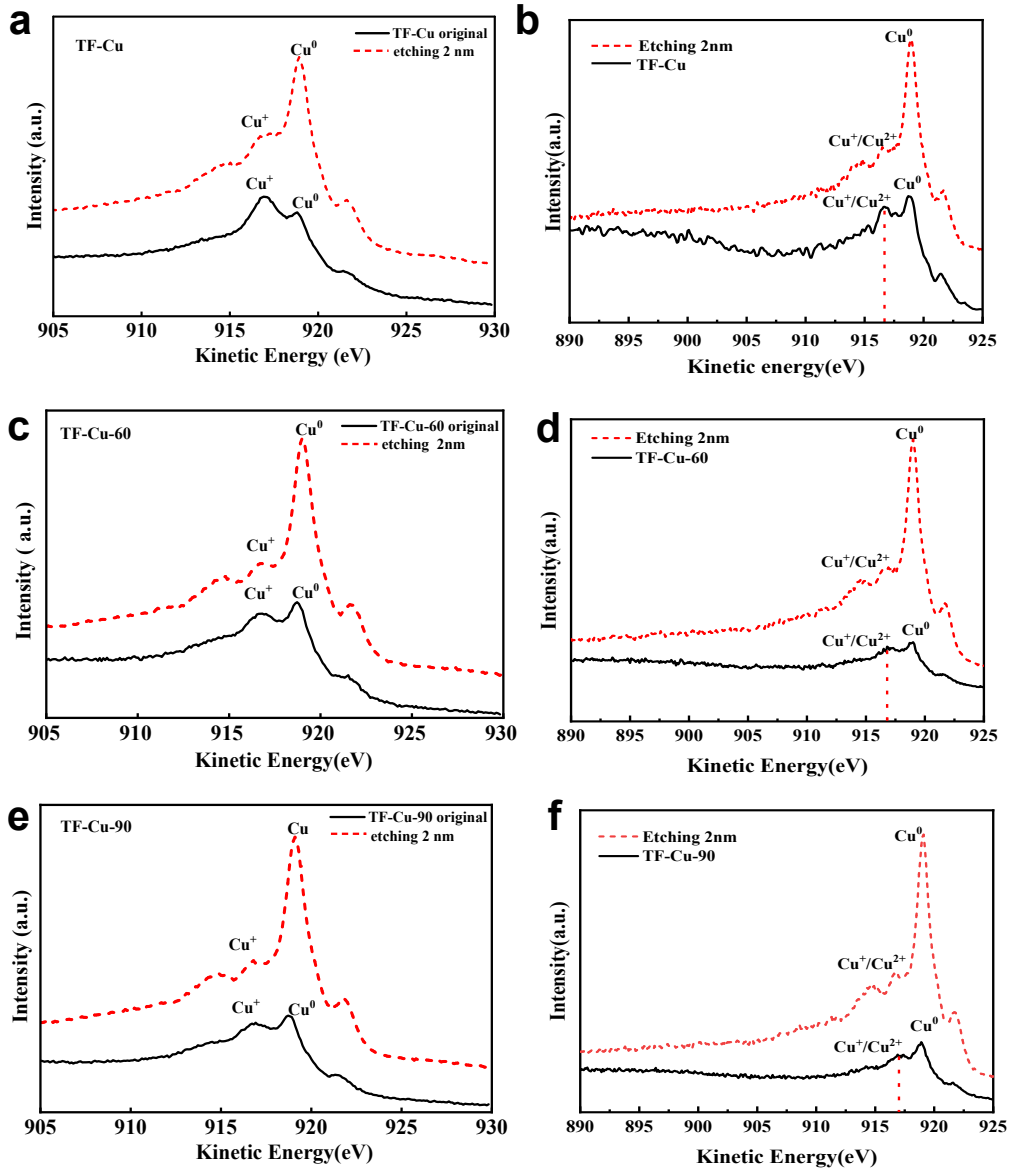

Fig. S8 AES of TF-Cu under different annealing times. (a,c,e). The AES of TF-Cu, TF-Cu-60, and TF-Cu-90 before reaction, respectively. (b,d,f). The AES of TF-Cu, TF-Cu-60, and TF-Cu-90 after reaction, respectively.

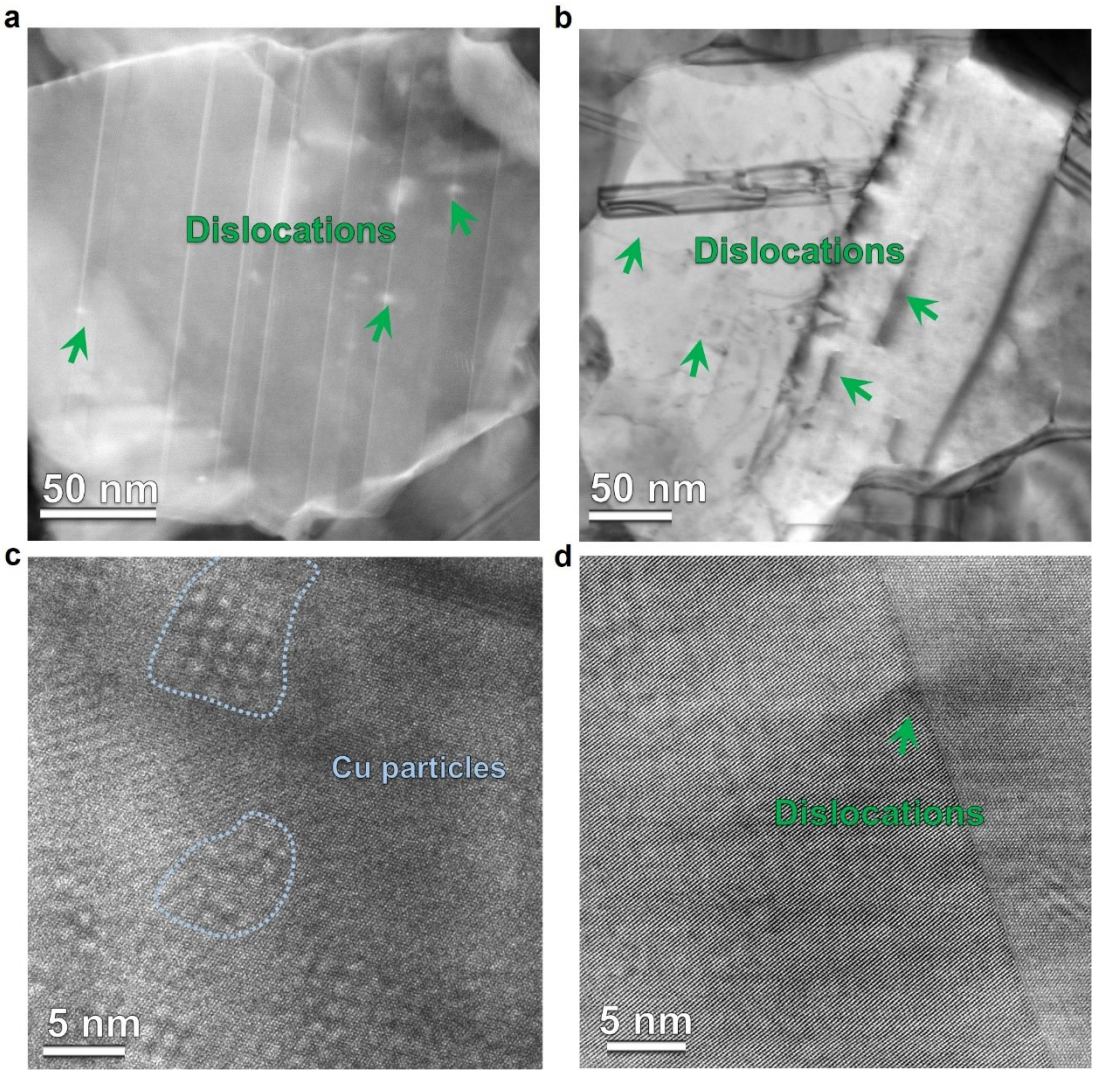

Fig. S9 (a)The SEM images showing the surficial morphology of TF-Cu catalyst before and after reaction. (b) Low magnification HAADF-STEM image of the TF-Cu-90 after reaction. Green arrows were used to outline numerous dislocation defects formed within Cu grains, which resulted from the formation of stress of grain growth. (c,d) The atomic-scale HAADF-STEM image of the TF-Cu-90 after reaction. The Moiré pattern in the image can be determined from the EDS analysis of S10 to be formed by the superposition of copper particles and the copper substrate.

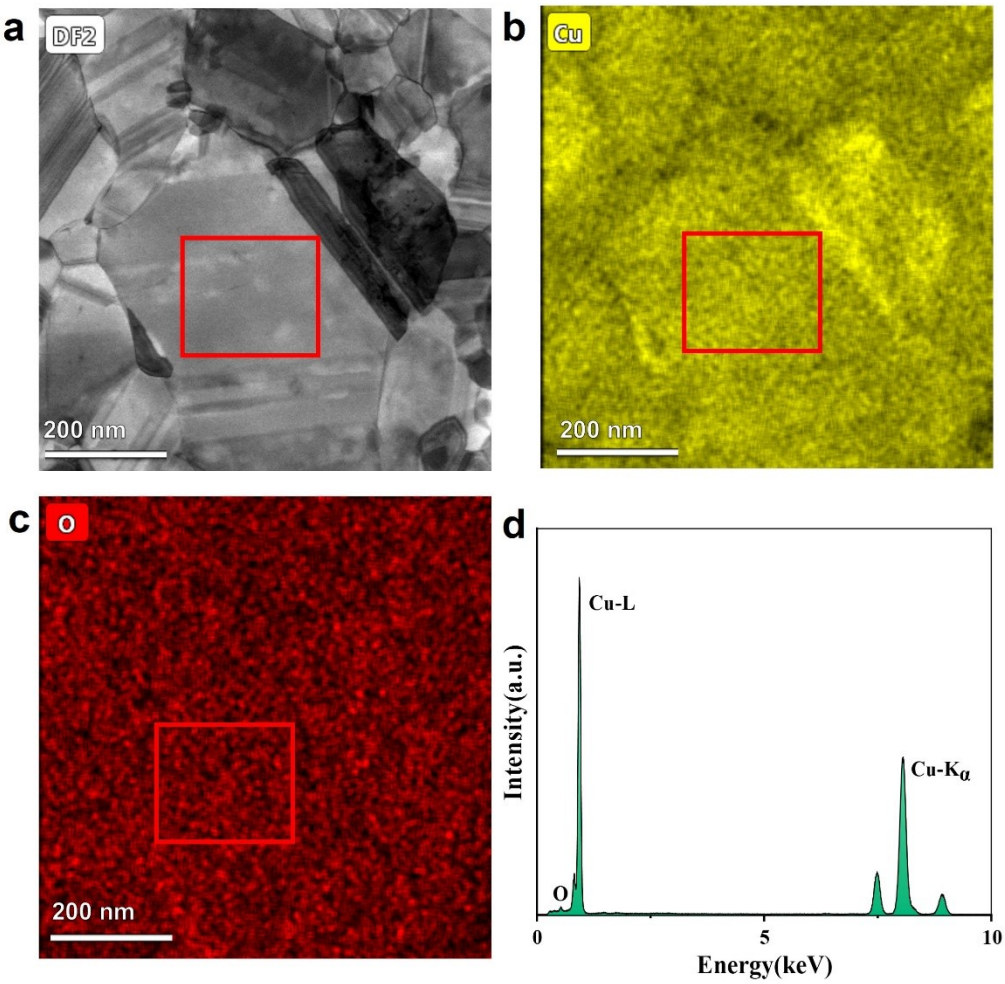

Fig. S10 (a-c) The DF2-STEM image and corresponding EDS images of Cu and O elements of the TF-Cu-90 catalyst after 1h reaction. (d) The EDS spectrum of the red box region in Fig.S10a. It is seen that no clear O peak can be detected. And quantitative analysis revealed that the average content of Cu and O elements are 98.2% and 1.8% respectively, which is lower than the detection limit.

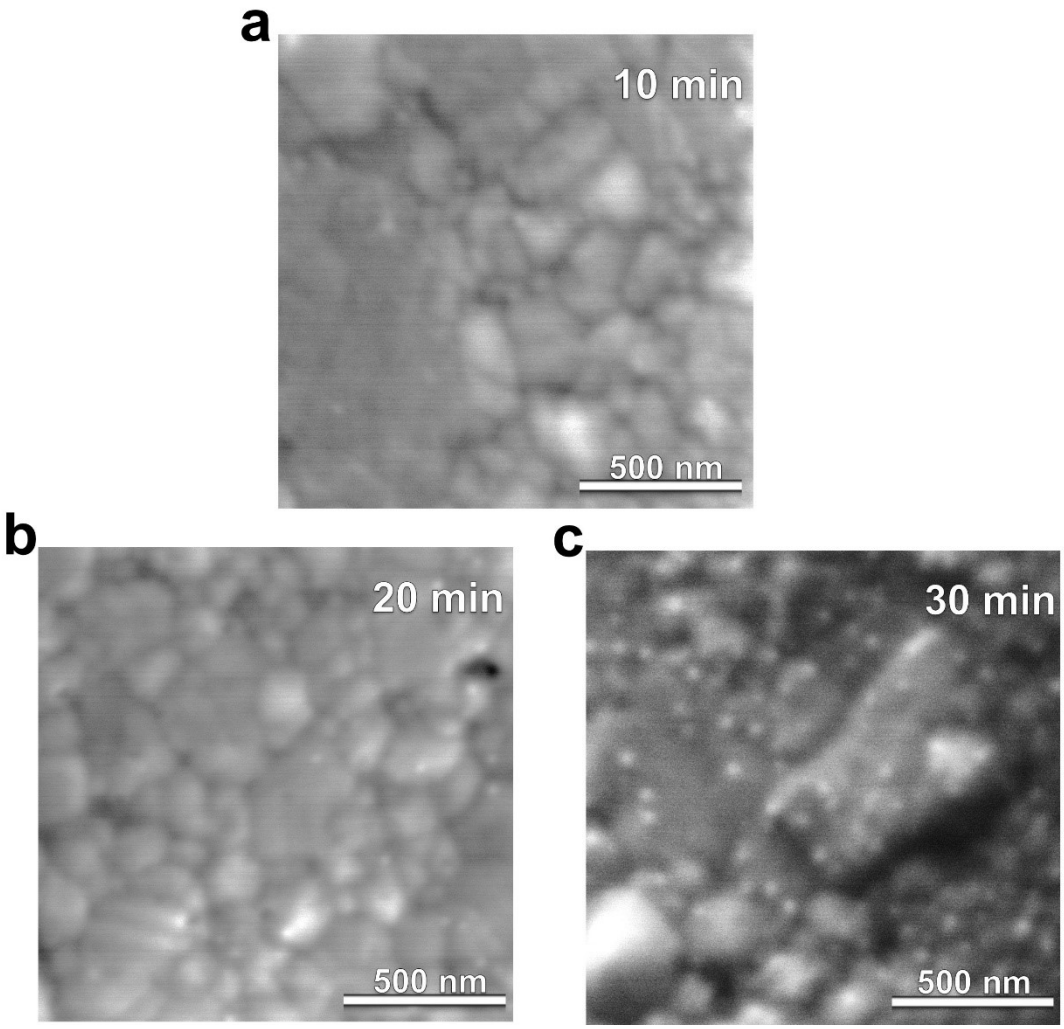

Fig. S11. SEM images of TF-Cu catalysts during different reaction times.

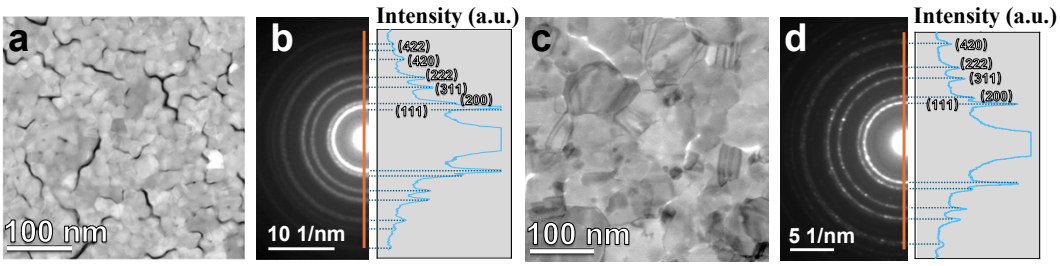

Fig. S12 (a,c) The HAADF-STEM images of pristine and heated treatment (300oC for 1 h) Cu films. (b,d) corresponding selected area electron diffraction images and intensity profiles. Fig. S12a and b show the STEM images of the original TF-Cu catalyst and corresponding selected area electron diffraction (SAED) patterns. Careful indexations reveal that all the diffraction rings can match well with the FCC Cu diffraction crystallography planes. The broad and diffused rings accompanied by weak discrete spots indicate a polycrystalline structure with small grains and limited local ordering. After in-situ heating for 1h at 300 °C (Fig. S12c and d), significant grain growth and clear twin structures are observed. The SAED patterns show brighter spots and rings, indicating the enhanced crystallinity.

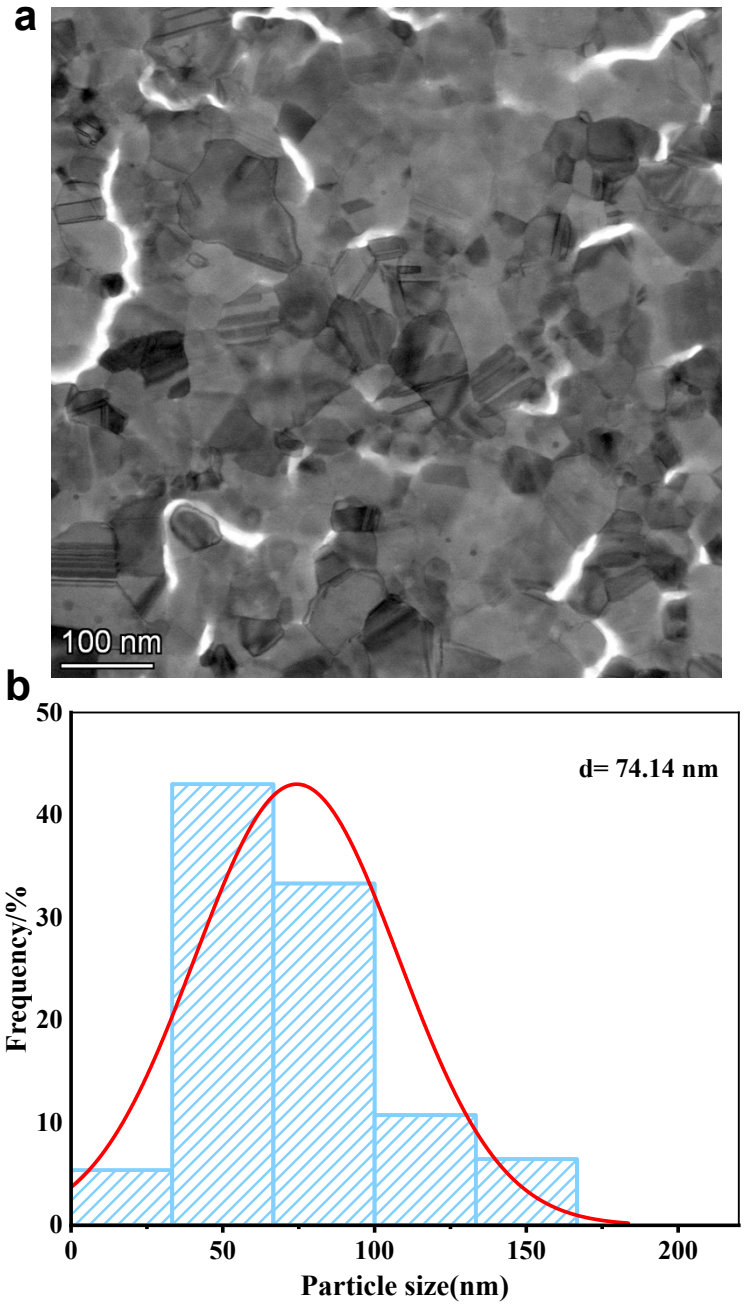

Fig. S13 (a) DF2-STEM image of TF-Cu catalyst after in-situ heating at 300 °C for 1h. (b) The corresponding grain size distribution.

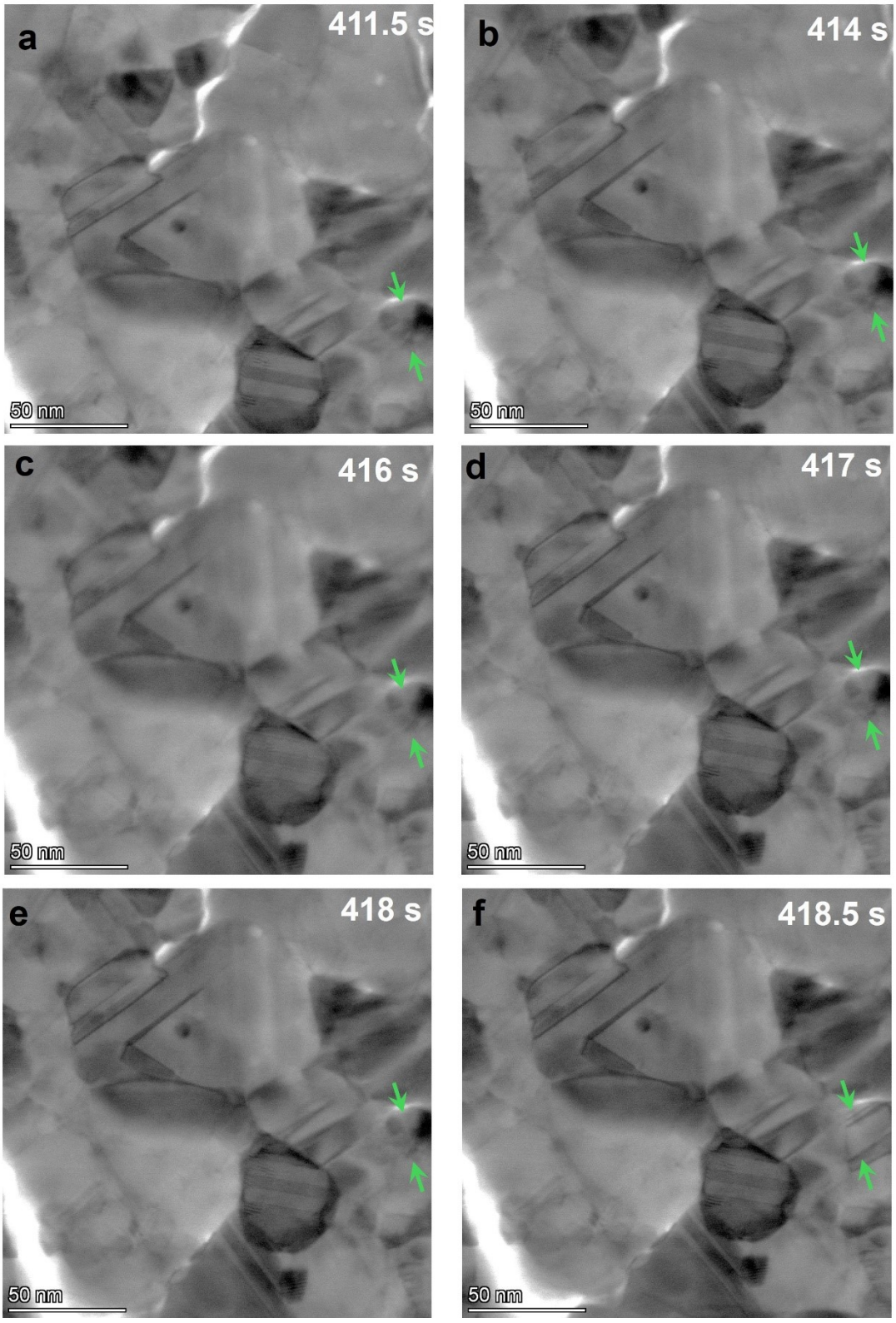

Fig. S14 In-situ DF2-STEM observations of the twin boundary formation.

Table S1 Particle size statistic of different annealing times of TF-Cu

	Diameter/nm	Mean/nm	Amount	Frequency/%
TF-Cu	15-18	16.35	3	1.50%
	18-20	19.05	20	10.00%
	20-23	21.75	43	21.50%
	23-26	24.45	47	23.50%
	26-29	27.15	42	21.00%
	29-31	29.85	28	14.00%
	32-42	35.25	17	8.5%
TF-Cu-60	23-42	32.55	16	15.53%
	42-60	51.65	30	29.13%
	60-80.	70.75	26	25.24%
	80-100	89.85	13	12.62%
	100-120	108.95	9	8.74%
	120-140	128.05	2	1.94%
	140-214	185.35	5	4.85%
TF-Cu-90	32-60	46.70	18	16.07%
	60-90	76.00	31	27.68%
	90-120	9.32	20	17.86%
	120-150	9.30	9	8.04%
	150-180	8.76	12	10.71%
	180-208.	9.20	10	8.93%
	208-326	252.50	12	10.72%

Table S2 The density of the twin boundary in Fig. S2d.

	Length (μm)	Area (μm^2)	Density (μm^{-1})
TF-Cu-0	3.59	9	0.399
TF-Cu-60	7.11	8	0.889
TF-Cu-90	17.44	8	2.180